

Qualitative Analysis of the Time-Frequency Signature Induced by a Reflected L-Band Signal from Time Evolving Sea Surfaces

Arnaud Coatanhay and Alexandre Baussard

¹*ENSTA Bretagne / Lab-STICC (UMR CNRS 6285), Brest, France*

(Dated: December 17, 2013)

Abstract

Passive remote sensing techniques have become more and more popular for detection and characterization purposes. The advantage of using the Global Navigation Satellite Systems (GNSS) are the well known signals emitted and the availability in most areas on Earth. In the present paper, L-Band signals (including GNSS signals) are considered for oceanographic purposes. The main interest in this contribution is the analysis of the signal reflected by an evolving sea surface using time-frequency transforms. The features which occur in this domain are examined in relation to the physical phenomena: interaction of the electromagnetic waves with the moving sea surface.

1 Introduction

For a decade, the passive remote sensing techniques based upon electromagnetic sources of opportunity have become more and more popular for detection and characterization purposes. The most significant reason for this enthusiasm lies in the fact that the passive systems take advantage of the numerous existing electromagnetic emitting sources to come up with new approaches for remote sensing or surveillance applications. As a matter of fact, among all the possible sources of opportunity, the Global Navigation Satellite Systems GNSS (GPS, GALILEO, GLONASS,...) appear among the most relevant solutions since the electromagnetic signals emitted (in L-Band) are reliable, available all over the world, deterministic and perfectly known (for direct paths).

It is worth noting that the use of GNSS signals for passive observation has been applied to a significant extent to the field of oceanography since the year 2000. Indeed, several studies have been carried out to estimate oceanographic parameters using the reflected GNSS signals measured from ground-based systems, see for example [1, 2], or airborne systems, see for example [3, 4, 5, 6]. These systems can be used for the measurement of wind velocity and wind direction [7, 8, 4, 9], surface roughness and its effects [3, 10, 5] or even to estimate the salinity [2].

For airborne and long range systems, the precision in time involves that the resolution cell easily exceeds a few hundred square meters in surface area. Then, the scattering by each individual sea wave can not be discriminated and described. In these cases, the sea surface is considered as a very large stochastic rough surface induced by the complex interaction between the fluid and the wind. In this context, the reflected GNSS is mostly seen as a tool to extract the statistical characteristics of a maritime environment (root mean square deviation of the sea surface height for instance).

For ground-based systems (see [1] for instance), the studies mainly focus on the delay/Doppler analysis of the GPS signals. The modulation of the GPS signal makes the sharp analysis on long coherent period quite difficult and limits the resolution in the time frequency domain.

The recent Maritime Opportunity Passive Systems (MOPS) [11] research project considers a local maritime domain observed in the vicinity of the sea surface. The prime objective of this project is to obtain a very high resolution analysis (very long coherent period and high precision in time) of the GPS phase for the direct and reflected signals in order to estimate the sea surface movements. From preliminary studies it appears that the obtained delay/Doppler maps show quite complex patterns that remain difficult to interpret. However, these patterns clearly suggests that this passive GNSS system should be able to detect the movement of individual sea waves.

The general purpose of this paper is closely related to this research project. It investigates the possibility of observing the movement and the deformation of a sea surface from the reflected signal in L-Band. In practice, we investigate the connections between a deterministic time evolving surface and the time-frequency representation of the signal scattered by this surface. The idea is to take advantage of these representations to extract oceanographic parameters from Doppler and micro-Doppler signatures. In a broad outline, a sea surface can be seen as a sum of ‘sinusoidal’ surfaces at several scales. Basically, it can be expected that the

large scale, corresponding to the gravitational waves, will be related to the global motion of the sea and the small scales, corresponding to the capillary waves directly induced by the wind, to the roughness of the sea surface.

In this paper, we will concentrate on the interpretations of the time-frequency signatures of the signal scattered by the evolving sea surface. These interpretations should be of a great importance for complementary works dealing with the estimation of oceanographic parameters. We can expected to estimate, as already noted, the movements and the deformations of a sea surface (i.e. the local sea state and the sea roughness) but also the local wind velocity and direction.

First, our approach consists in generating time evolving (two-dimensional) surfaces and computing the field of a plane wave in L-Band scattered by these surfaces. The numerical model is based upon the Method of Moment (MoM) which is a standard approach used to quantify the scattering by sea surfaces, in L-Band. Then, the time-frequency signatures of the scattered signal are obtained using Wigner-Ville representations. Finally, making comparisons with the signatures produced by canonical surfaces (moving sinusoids for instance), we provide interpretations of the complex signatures corresponding to more realistic sea surfaces.

The sequel of the paper is organized as follows. In Section 2 the electromagnetic model used to compute the scattered electromagnetic field is introduced. Section 3 describes the model applied to generate realistic evolving sea surfaces. Then, Section 4 presents a short overview of the time-frequency representations used in this paper. Sections 5 and 6 give an interpretation of the time-frequency representations of the signal reflected from canonical and modeled sea surfaces. Finally, Section 7 gives some concluding remarks and proposes some future works dealing with the extraction of the characteristics of the sea surface from the time-frequency representations.

2 Electromagnetic model

Roughly speaking, the GNSS signal can be considered as a plane Right Hand Circular Polarization (RHCP) incident wave. For the sake of simplicity, we assume in the following that the satellites are at the Zenith position, so the incident wave propagates in the Nadir direction, see Figure 1.

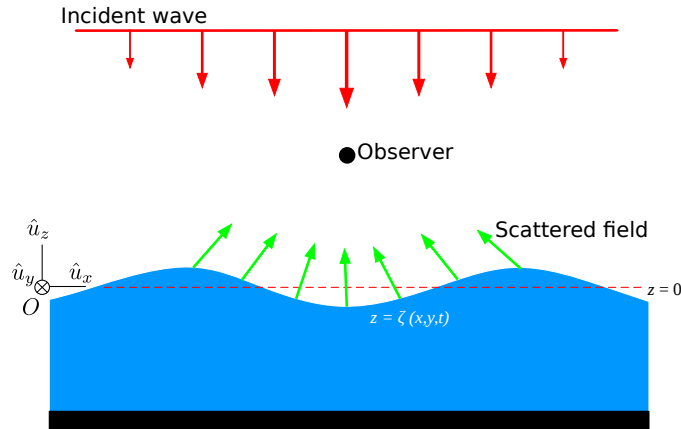


Figure 1: Geometrical configuration.

In this configuration, the electromagnetic modeling consists in the evaluation of the scattering of a plane RHCP wave by a dielectric interface. As a matter of fact, due to the salinity of the sea water, the surface is assumed to be a Perfect Electric Conductor (PEC). It is noteworthy that a circular polarized plane wave can be split into two linear polarized plane waves: Transverse Magnetic (TM) and Transverse Electric (TE) polarization. An appropriate approach to modeling the scattering by TM and TE polarized wave is to consider the Boundary Integral Equation Method (BIEM) and the estimation using functional basis: Method of Moments (MoM).

For the TM polarization ($\vec{E} = E\hat{u}_y$), the modeling of the scattering is based upon the Electric Field Integral Equation (EFIE) [12]:

$$E_y^{inc}(\vec{\rho}) = i\omega_{em}\mu \int_{\Gamma} J_{TM}(\vec{\rho}') G(\vec{\rho}, \vec{\rho}') d\vec{\rho}', \quad (1)$$

where E_y^{inc} is the incident field, μ is the permeability of free space, Γ represents the sea surface, ω_{em} is the angular frequency of the electromagnetic wave, J_{TM} is the surface current, $G(\vec{\rho}, \vec{\rho}')$ is the 2D Green function, $\vec{\rho}'$ and $\vec{\rho}$ are the source and observation points on the sea surface ($\vec{\rho}', \vec{\rho} \in \Gamma$). It is worth noting that the incident wave is known and is assumed to be tapered to avoid numerical truncation effects. So, the amplitude E_y^{inc} of incident field will be given by [13]:

$$E_y^{inc}(x) = e^{-ikz(1+v_t(x))} e^{-\frac{x^2}{g_t^2}}, \quad (2)$$

where g_t is the tapering parameter and the additional factor in the phase v_t is:

$$v_t(x) = \frac{\left[2\frac{x^2}{g_t^2} - 1\right]}{(kg_t)^2}. \quad (3)$$

The 2D Green function $G(\vec{\rho}, \vec{\rho}')$ is also perfectly known, and the only unknown function of the integral equation (1) is the surface current J_{TM} . When the surface is computed, the scattered field is determined using the following relation:

$$E_y^{scat}(\vec{\rho}_{obs}) = -i\omega_{em}\mu \int_{\Gamma} J_{TM}(\vec{\rho}') G(\vec{\rho}_{obs}, \vec{\rho}') d\vec{\rho}', \quad (4)$$

where $\vec{\rho}_{obs}$ is the position of the observer above the sea surface.

For the TE polarization, the electrical field \vec{E} belongs to the plane $(O, \hat{u}_x, \hat{u}_z)$ and the magnetic field is in the form ($\vec{H} = H_y\hat{u}_y$). So the modeling of the scattering in TE polarization is based upon the Magnetic Field Integral Equation (MFIE)[12]:

$$H_y^{inc}(\vec{\rho}) = -\frac{J_{TE}(\vec{\rho})}{2} + \int_{\Gamma} J_{TE}(\vec{\rho}') [\hat{n}(\vec{\rho}') \nabla' G(\vec{\rho}, \vec{\rho}')] d\vec{\rho}', \quad (5)$$

where $\hat{n}(\vec{\rho})$ is the normal vector to the sea surface at the position $\vec{\rho}$, $\nabla' G(\vec{\rho})$ is the gradient related to the second variable of the Green function, H_y^{inc} is the incident field and J_{TE} is the surface current.

In the same way as the TM polarization case, the integral equation (5) determines the surface current J_{TE} . So, the magnetic field \vec{H} received by the observer is computed using a relation similar to equation (4), and then the electric field received by the observer can be evaluated.

Considering both TM and TE polarizations and a standard Method of Moment (MoM) approach to solve the integral equations (1 and 5) (a detailed presentation can be found in [14]), we can simulate the scattering of a GNSS signal (RHCP plane wave) by a sea surface.

The last point for the electromagnetic modeling that needs to be said is that the receiver antenna of the observer is Left Hand Circular Polarized (LHCP) to optimize the recording of the reflected signal. So the actual received signal will be the LHCP component of the scattered field.

3 Sea surface model

Since the previously described electromagnetic model estimates the scattered field for any surface, the last step to obtain a complete simulation is the generation of the sea surfaces. Physically, a sea surface is induced by a complex and stochastic interaction between the fluid and the wind. Fortunately, a statistical description of the energy spectral decomposition of the sea surface can be approximated by empirical and/or semi-theoretical models for different wind speeds and wind directions. One of the most consistent with the experimental data has been developed by Elfouhaily et al. [15]. This sea spectrum is in the form:

$$S(K_{sea}, \phi) = M(K_{sea})f(K_{sea}, \phi_{sea}), \quad (6)$$

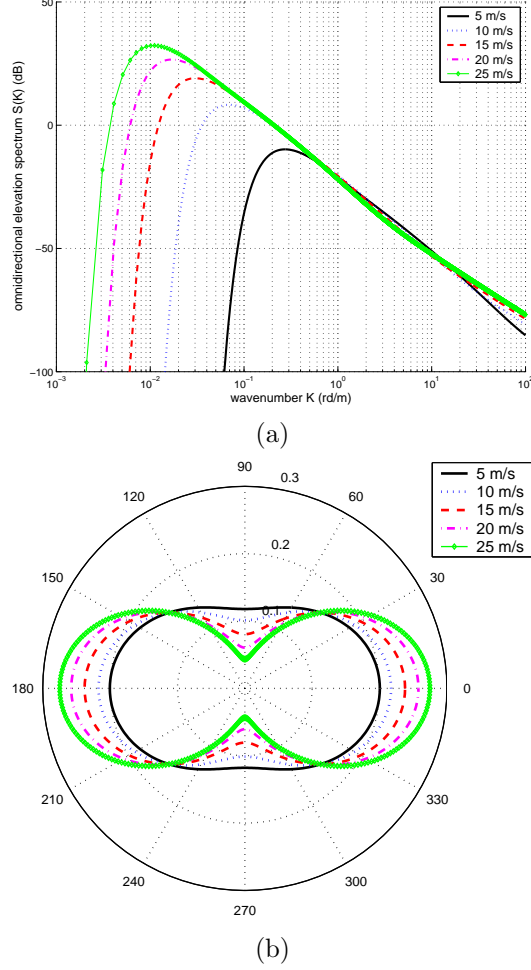


Figure 2: Elfouhaily sea surface spectra with different wind speeds: (a) Omnidirectional elevation spectrum component (b) Angular function component.

where $M(K_{sea})$ represents the isotropic part of the spectrum modulated by the angular function $f(K_{sea}, \phi_{sea})$. K_{sea} and ϕ_{sea} respectively denote the spatial wave number and the wind direction, see Figure 2.

To generate a realistic sea surface associated to a given weather condition (wind speed and wind direction), we expand the surface into a continuous sum of sinusoidal curves. For each spatial wave number K_{sea} , the mean amplitude is estimated using the square root of the sea spectrum and the phase is randomly set between 0 and 2π . In practice, the convolution of the square root of the spectrum with a unitary white Gaussian random signal generates a one-dimensional profile (a statistical realization of the sea surface) that represents an ocean surface for given weather conditions.

To describe the time evolution of the sea surface thus obtained, we associate a time wave number $\omega_{sea}(K_{sea})$ for each K_{sea} using the phase dispersion relation:

$$\omega_{sea} = \sqrt{g_g K_{sea} \left(1 + (K_{sea} A)^2\right)}, \quad (7)$$

where g_g is the acceleration due to gravitation and A is the amplitude of the sinusoidal curve.

Finally, we can generate a realistic time-evolving surface and using the electromagnetic model we can also estimate the signal recorded by the receiver. Now, we will demonstrate that these simulated signals analyzed with time-frequency tools lead to many physical interpretations.

4 Time-Frequency overview

The numerical simulation of the electromagnetic waves intercepted by an observer above a time-varying sea surface provides complex non-stationary signals. A relevant approach to fully describe the nature of these non-stationary signals consists in a Time-Frequency (TF) analysis.

Indeed, a Time-Frequency Distribution (TFD) shows how the spectral content of the signal evolves with time, thus providing an ideal tool to dissect, analyze and interpret non-stationary signals. Most of time, the Time-Frequency Distribution (TFD) maps the energy of a one-dimensional time-domain signal into a two-dimensional function of time and frequency.

In this article, we will stress the fact that the feature extraction based on time-frequency analysis of an electromagnetic field above the sea can be exploited to point out useful information about the signal fluctuation induced by the movement of the surface.

A great variety of methods for obtaining a TFD have been defined, most notably the short time Fourier transform, the wavelet transform and the Wigner-Ville distribution. For more details the reader can refer for example to [16] and the Time-Frequency Toolbox (TFTB¹). This article deals with the Wigner-Ville distribution.

4.1 The Wigner-Ville Distribution

The Wigner-Ville Distribution (WVD) of a signal $y(t)$, denoted by $W_z(t, f)$, is defined as

$$W_z(t, f) = \int_{-\infty}^{\infty} z(t + \tau/2)z^*(t - \tau/2)e^{-j2\pi f\tau}d\tau, \quad (8)$$

where $z(t)$ is the analytic associate of $y(t)$ (i.e the Hilbert transform of the real signal $y(t)$).

The main properties of the WVD are : it is always real-valued, it preserves time and frequency shifts and it satisfies the marginal properties.

Unfortunately, the WVD shows interference terms. These interference terms are troublesome since they may overlap with signal terms and thus make it difficult to visually interpret the WVD image. Basically, the interference between two points in the time-frequency plane correspond to the appearance of a third point located at the geometrical midpoint. Besides, the interference terms oscillate perpendicularly to the line joining the two interfering points, with a frequency proportional to the distance between these two points.

In order to reduce the interference terms, the Pseudo-Wigner-Ville Distribution (PWVD) can be used. This transform is described in the following.

4.2 The Pseudo-Wigner-Ville Distribution

The PWVD is defined as

$$PW_z(t, f) = \int_{-\infty}^{\infty} h(\tau)z(t + \tau/2)z^*(t - \tau/2)e^{-j2\pi f\tau}d\tau, \quad (9)$$

where $h(\tau)$ is a regular window.

This windowing is equivalent to a frequency smoothing of the WVD. It leads to the attenuation of the interference terms. However, an excessive window leads to a loss in properties and may damage the joint-time-frequency resolution.

5 Reflected signal in the TF domain - canonical surfaces

As already mentioned, the electromagnetic field scattered by a realistic time-varying sea surface induces complex non-stationary signals received by the observer. So, in a first phase, we suggest generating and analyzing the received signal when the simulated sea corresponds to a canonical moving surface (a sinusoid for instance).

¹<http://tftb.nongnu.org/>

| Scale | Description | wind speed (m/s) | Amplitude (m) | Wavelength (m) | velocity (m/s) |
|-------|--------------------|---------------------|------------------|-------------------|-------------------|
| 1 | Light air | 0.3-1.5 | 0.0-0.012 | 0.4-2.44 | 0.8-1.95 |
| 2 | Light breeze | 1.6-3.3 | 0.014-0.12 | 2.77-11.8 | 2.08-4.29 |
| 3 | Gentle breeze | 3.5-5.4 | 0.15-0.54 | 13.3-31.6 | 4.55-7.02 |
| 4 | Moderate breeze | 5.5-7.9 | 0.57-1.70 | 32.8-67.8 | 7.15-10.27 |
| 5 | Fresh breeze | 8-10.7 | 1.77-4.23 | 69.4-124.3 | 10.4-13.9 |

Table 1: Sinusoidal sea surface parameters.

In this section, we will attempt to provide several interpretations of the time-frequency signatures for simple or more sophisticated canonical reflecting surfaces. This step strikes us as necessary to understand and explain the main features obtained in the time-frequency domain for more complex reflecting surfaces. In what follows, we will consider the increasing complexity of the simulated reflecting surface: from the case of a simple sinusoidal surface to the case of the linear superposition of several sinusoidal surfaces.

5.1 Main parameters of the canonical surfaces

Let the sea surface be approximated, for its global shape and motion, by a simple sinusoid s defined as

$$s(t, x) = A_{sin} \sin(-\omega_{sin} t + k_{sin} x). \quad (10)$$

The main parameters of this surface are the amplitude A_{sin} , the velocity c_{sin} , the angular frequency $\omega_{sin} = 2\pi f_{sin}$ or the wavelength $\lambda_{sin} = c_{sin}/f_{sin}$ and the wavenumber $k_{sin} = 2\pi/\lambda_{sin}$. In (10), t stands for the time and x for the position. To come closer to a realistic sea model, the parameters of this sinusoidal model should be inferred from the sea surface model introduced in Section 3.

For given weather conditions (wind speed and wind direction), the wavenumber of the sinusoid k_{sin} is fitted to the abscissa $K_{sea, max}$ of the maximum of omnidirectional elevation spectrum component, see Figure 2. Since the wavenumber k_{sin} is set, the angular frequency ω_{sin} can be computed using the phase dispersion relation (7). The wavelength λ_{sin} and the velocity c_{sin} can then be deduced.

To determine the amplitude of the sinusoid, we generate realistic sea surfaces from the Elfouhaily spectrum. Then, the standard deviation σ_{sea} of the wave height is computed. In physical oceanography, the global characteristic is given by the Significant Wave Height (SWH or H_s) which is defined traditionally as the mean wave height (trough to crest) of the highest third of the waves ($H_{1/3}$). In practice, the SWH is usually defined as four times the standard deviation of the surface elevation: $SWH = 4\sigma_{sea}$. This is why the sinusoid amplitude is set to $A_{sin} = 2\sigma_{sea}$.

The estimated parameters defining the sinusoidal surfaces are given in Table 1. Note that, in this paper, only the Beaufort scales from 1 to 5 are considered.

These simplifying assumptions and the estimated parameters have been experimentally validated by comparing the obtained evolving sinusoidal surfaces, for several values of the Beaufort scale, with the global shape and motion of several sea surfaces (generated using the Section 3 model) at the same Beaufort scales. Figure 3 shows a 60m sinusoidal surface at time t and the corresponding sea surface for scale 3. The main visual difference is the wavelength of both surfaces. It clearly appears from Figure 3 that the canonical surface corresponds to only one wavenumber and the simulated sea surface to a mixture of a wide frequency spectrum. However, the sinusoidal surface obtained remains broadly an acceptable model in the first instance.

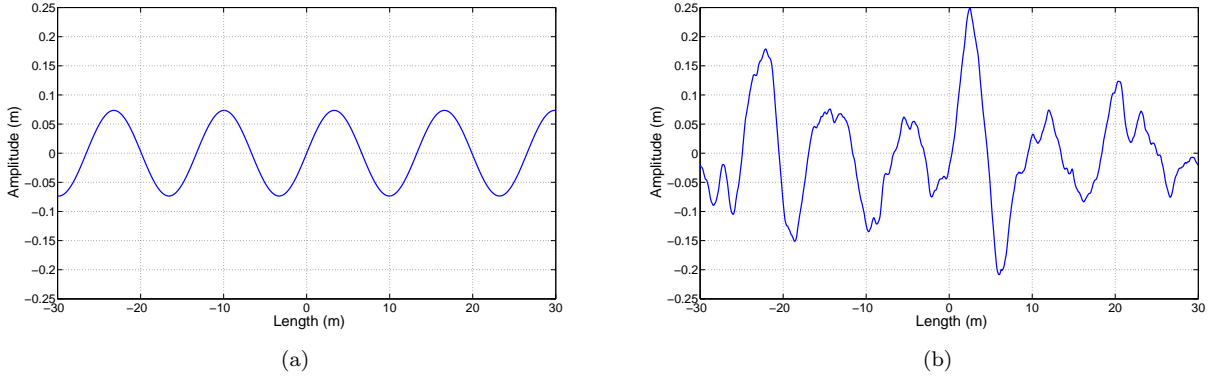


Figure 3: Generated (a) pure sinusoidal surface and (b) sea surface for a Beaufort scale 3.

5.2 Simulation for a pure sinusoidal surface

Considering the previous sinusoidal surface and the electromagnetic model presented in Section 2, we are able to simulate the signal measured at the receiver over a period of 16s. Then, applying a Pseudo-Wigner-Ville Distribution (PWVD), a two-dimensional representation of this signal can be achieved in the time-frequency domain. Figure 4 presents the time-frequency representation of the received signal reflected from surfaces corresponding to the levels 2, 3 and 4 in the Beaufort scale.

At first sight, the time-frequency feature seems very close to a sinusoid. This is mainly due to the fact that the scattering phenomenon becomes time-periodic in the case of a sinusoid surface. Nevertheless, a closer examination shows that the time-frequency feature looks more like a distorted sinusoid, see Figure 5. We must not forget that the TF representation shows the variations of the Doppler frequency observed by the receiver induced by the motion of the sinusoid surface. Finding the relation between the evolving sea surface elevation and the Doppler variations is the key challenge in analyzing the PWVD and interpreting the time-frequency signature.

In order to give a useful interpretation, let us denote by P_1 , P_2 , P_3 and P_4 four significant points observed in the PWVD of the signal received for a sinusoid surface, see Figure 5. The abscissa of these points are the time delays $t_1 = 5.10s$, $t_2 = 5.98s$, $t_3 = 6.56s$ and $t_4 = 7.13s$. The points P_2 and P_4 respectively correspond to a maximum and a minimum of the time frequency signature and the points P_1 and P_3 correspond to two Doppler zero-crossings.

The Doppler frequency is zero (P_1 and P_3) when a maximum or a minimum of the sinusoidal surface is under the receiver position (see Figure 6). In fact, due to the tapering of the incident field, the incident wave mainly impinges on central area of the sea surface and using the approximation of the ray theory, the main electromagnetic contribution coming from the sea surface is induced by the specular point situated at the top (or the bottom) of the sea surface, see Figure 7. The velocity associated to this specular point (red arrow in Figure 7) is strictly perpendicular to the observer direction, so the Doppler shift is zero. Note that in Figure 7, and also in Figure 8, the black arrows stand schematically for the intensity (length of the arrow) and direction of the incident wave.

Numerically, if we remember that the wavelength of the sinusoidal surface is $\lambda_{sea} = 13.3m$, the velocity is $c_{sea} = 4.55m/s$ and the time period is $T_{sea} = 2.92s$, we note that $t_3 - t_1 = 1.46s$ exactly corresponds to half of the T_{sea} period.

On the other hand, the Doppler frequency is maximal or minimal (P_2 and P_4) when the amplitude (see Figure 6) of the sinusoidal surface above the observer is close to zero (i.e. the inflexion point of the sinus). Figure 8 illustrates this configuration and shows the velocity vector at this point.

However, the extrema of the Doppler signature do not strictly correspond to the zero-crossings of the sea surface, and $t_4 - t_2 = 1.15s \simeq 1.46s$ is an approximation of half of the T_{sea} period. Thus we can say that the Doppler signature is a distorted sinusoid. Furthermore, a simple calculation shows that the velocity vector at the point above the observer does not correspond to the Doppler shift at point P_2 or P_4 .

In the sequel, we show that it is possible to make a further, detailed analysis of the time-frequency

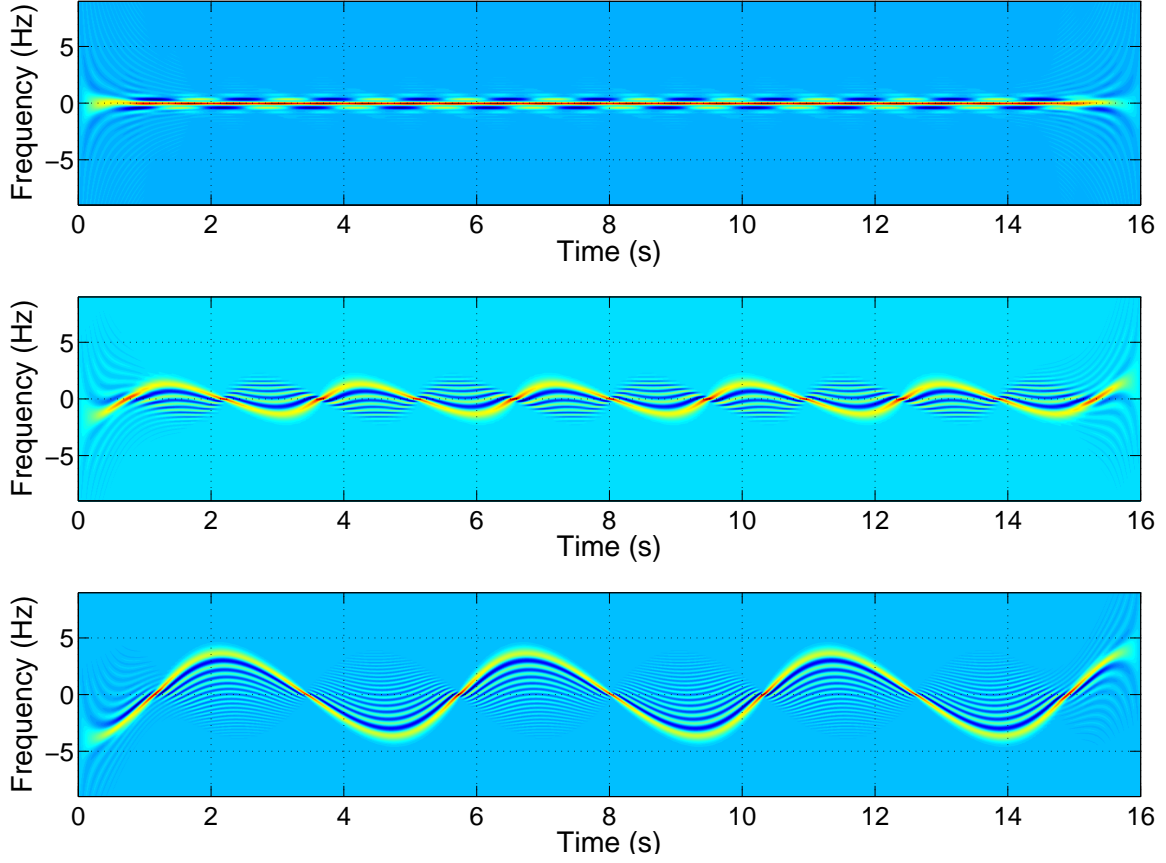


Figure 4: Time-frequency representation (with same color scale) of the received signal reflected by a sinusoidal surface with parameters corresponding to the Beaufort scales (top) 2, (middle) 3 and (bottom) 4.

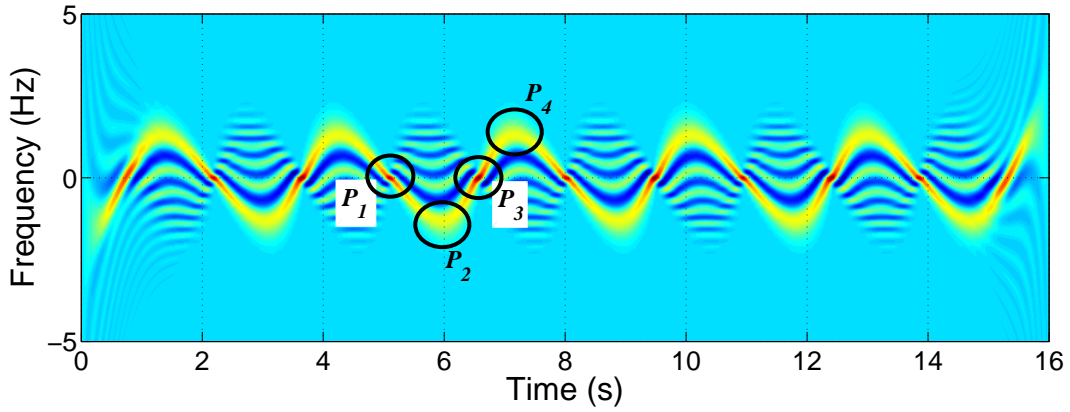


Figure 5: Zoom of Figure 4 (middle). The white circles point out the time-frequency signature at four different times: $t_1 = 5.10\text{s}$, $t_2 = 5.98\text{s}$, $t_3 = 6.56\text{s}$ and $t_4 = 7.13\text{s}$.

signature by drawing analogies from the ray theory and explaining the shape of the signature by the presence of specular points.

More precisely, the feature in the time-frequency domain for this kind of surface is due to the motion of the specular point which reflects maximum energy in the receiver direction. To illustrate this, Figure 9 shows the PWVD of the received signal after reflection on the sinusoidal surface and the evolution (black

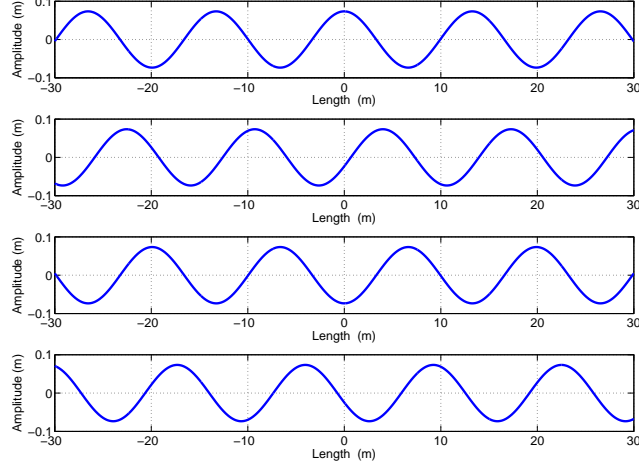


Figure 6: The sinusoidal sea surfaces at the four different times (top to bottom): $t_1 = 5.10\text{s}$, $t_2 = 5.98\text{s}$, $t_3 = 6.56\text{s}$ and $t_4 = 7.13\text{s}$.

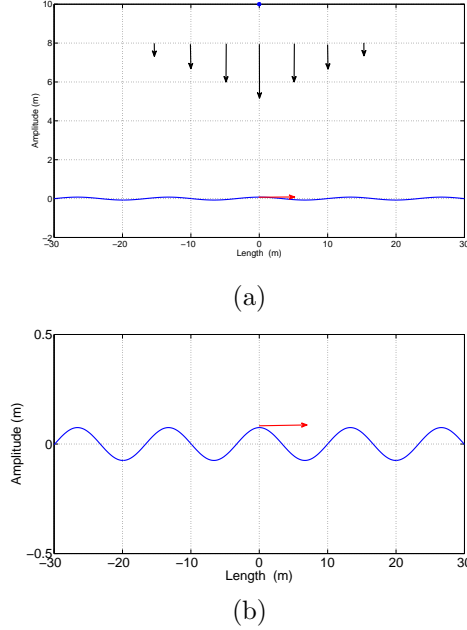


Figure 7: (a) Setup of the system at $t_1 = 5.10\text{s}$ (P_1), (b) zoom of (a).

line) of the Doppler frequency due to the single moving specular point (for the considered sinusoidal surface only one specular point exists at each time).

In practice, the specular point is geometrically determined in the central lobe of the incident wave and its Doppler frequency is computed as:

$$f_d(t) = \frac{1}{\lambda_{em}} \frac{d}{dt} (R_{ET} + R_{TR}), \quad (11)$$

where R_{ET} and R_{TR} are respectively the distances Emitter-Target and Target-Receiver.

At L-band, for a simple sinusoidal surface and the considered setup, the MoM model and the single point source (specular point) approximation have significant differences in quantitative terms. However, in terms of qualitative description, both approaches provide very similar time frequency signatures. This can be easily illustrated by generating the signal $V(t)$ measured at the receiver due to the specular point considered as a

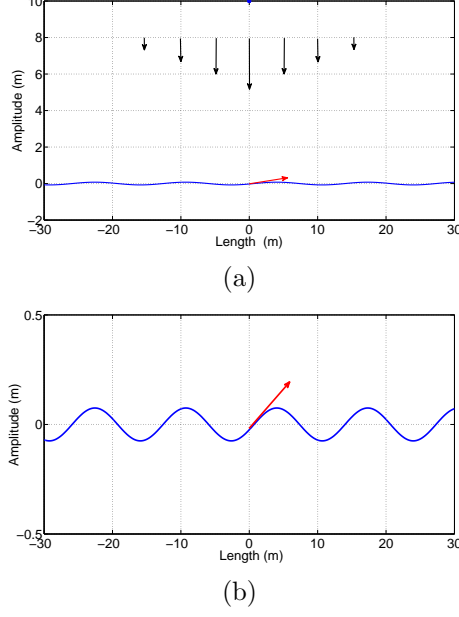


Figure 8: (a) Setup of the system at $t_2 = 5.98s$, (b) zoom of (a).

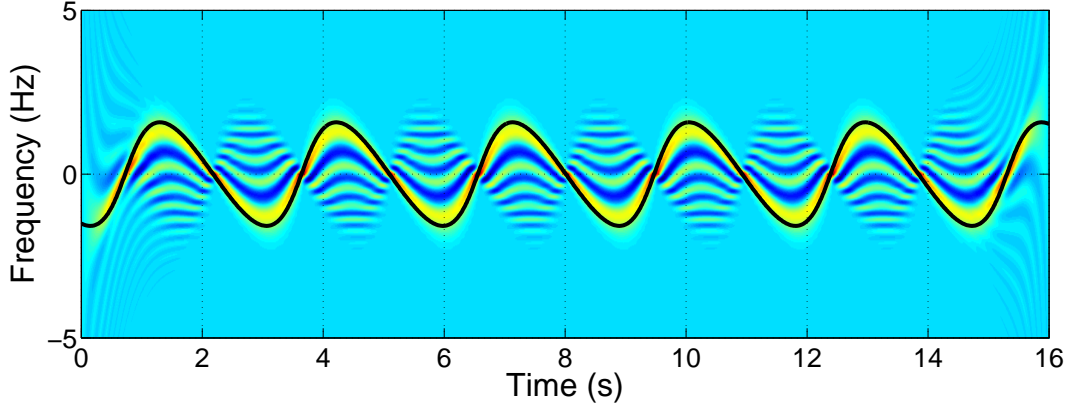


Figure 9: PWVD of the received signal and (in black) Doppler frequency of the moving specular point.

source point. This signal is obtained from

$$V(t) = \exp[j(2\pi f_{em}t - k_{em}r)], \quad (12)$$

where r is the distance covered by the electromagnetic wave, f_{em} the frequency of the incident wave and k_{em} the electromagnetic wave number.

Figure 10 shows the PWVD obtained using this ‘point source model’. The feature amplitudes are quite different since a basic source model does not take into account the complex phenomena of attenuation. Nevertheless, the PWVD in Figure 10 is very nearly comparable to that obtained in Figure 9.

Specifically, the specular point interpretation offers a more thorough and intuitive analysis of the sinusoid feature in the time-frequency domain (see Figure 11). Indeed, the Figures 12 show the different positions of the central specular point for a half and a full period. The cyclic movement of the specular point clearly appears. It should nevertheless be noted that the motion of the specular point follows an elliptical path with a non-uniform speed. The specular point travels at a lower speed in the vicinity of the top of the sinusoidal sea surface (P_1) than near the bottom (P_3).

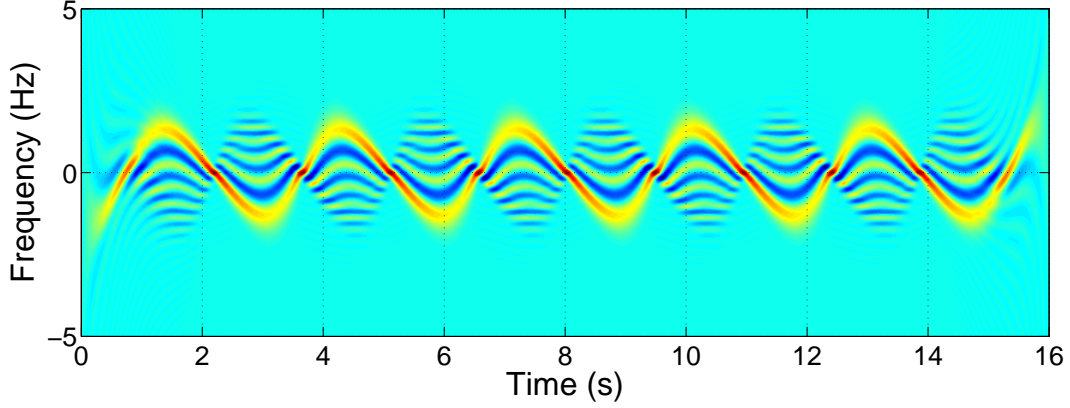


Figure 10: Time-frequency representation of the signal reflected by a sinusoidal surface using the point source model. To be compared with Figure 9.

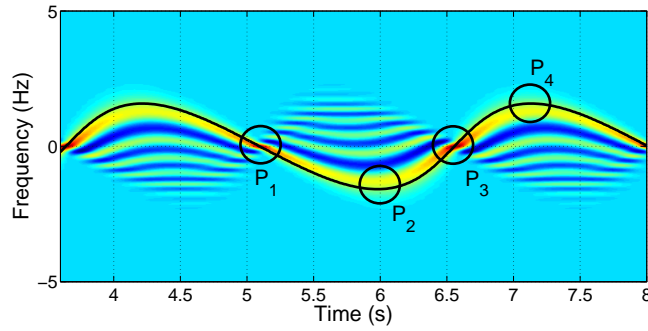


Figure 11: Zoom of the PWVD of the received signal (Figure 9).

Finally, the non-linear variations of the velocity when the specular point goes over the minima or the maxima of the sinusoidal surface is the reason for the time-frequency feature corresponding to a distorted sinusoid: $t_2 - t_1 > t_3 - t_2$.

5.3 Surface made of two sinusoids

Obviously, the monochromatic model of the sea surface is far from any acceptable level for a realistic interpretation. According to the spectral model of the sea surface previously presented (see Section 3), a sea is characterized by relevant physical phenomena at various scales: the surface with large wavelength and high amplitude stands for the gravity wave (large-scale roughness) and the surface with smaller wavelength and amplitude stands for the capillary and short gravity waves (small-scale roughness).

In order to come closer to reality, we consider the same previous sinusoidal surface to which a second sinusoid with smaller amplitude and wavelength is added. Figure 13 shows examples of such surfaces for a Beaufort scale 3. For this new generated surface, the parameters of the second sinusoid correspond to the amplitude of the first divided by three, the velocity remains the same and the wavelength is divided by four.

The time-frequency representation of the simulated signal obtained is given in Figure 14. In the same manner as outlined above, the two sinusoid models can lead to a specular point interpretation. Nevertheless, the sum of sine curves with different wavelengths involves local curvature phenomena and several specular points may appear in the central area. In Figure 14 (bottom) the Doppler frequencies associated to each specular point are superimposed (in black) on the time-frequency distribution. It is worth noting that they seem to generate a global continuous Doppler curve in the time-frequency domain. In Figure 15 we have highlighted the Doppler frequency associated with the present specular points at each time with different

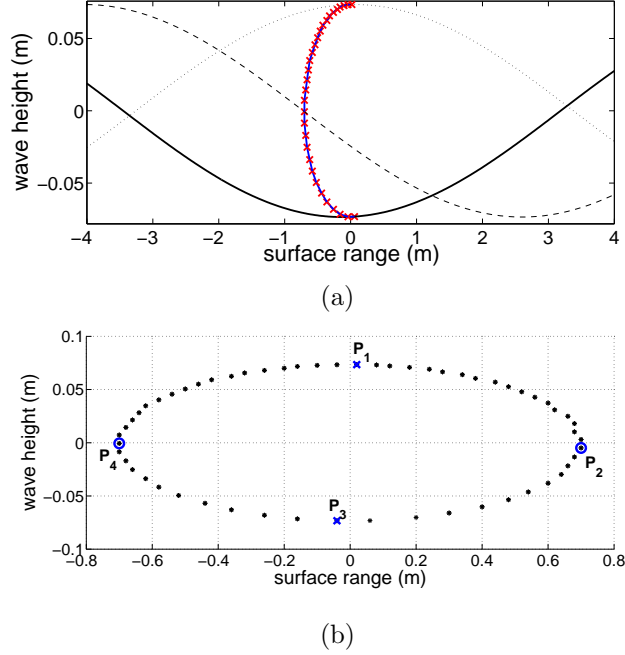


Figure 12: Evolution of the spatial positions of the specular points for (a) a half period and (b) a full period. In (a) the shape of the sinusoid surfaces (dashed and plain black lines) are presented at different times (beginning, middle and end of the half period) to show the coincidence with the specular point positions (red cross). In (b) the position of the specular points is given using black dots and particular positions are highlighted using blue circles and blue cross.

color. Moreover, the same color is used to highlight the motion of a given specular point throughout a period.

In Figure 14 (bottom) the evolution of the Doppler frequency due to the specular point in the monochromatic sea model (same as Figure 9) is also added in white. The Doppler curve due to the two sinusoids can be seen as the so-called [17, 18] micro-Doppler phenomenon (compare to the Doppler phenomena associated with the global signature due to the single sinusoid with larger amplitude). It appears clearly that there is a global trend highlighted by the white curve which is due to the motion associated with the main sinusoidal component (monochromatic model). In addition, the association of the two sinusoidal components induces oscillatory variations around this main trend.

In the present case, since the ratio between both sinusoids is an integer, the sea surface considered is deterministic and periodic. So, the TFR is also periodic. Let us consider a zoom into the TFR focusing on one period (see Figure 15). This can be associated with Figure 13 which shows the surface at several times and the position of the corresponding specular points (red star).

Closer examination of the time-frequency representation reveals the number of specular points and their motion. For instance, at the time $t = 3.78\text{s}$ (see Figure 15), three different intersections exist on the Doppler curve that can be related to the time-frequency components of three specular points, see Figure 13. On the other hand, at the time $t = 3.52\text{s}$, there is only one intersection on the Doppler curve, and there exists only one specular point, see Figure 13.

Despite the good agreement between MoM and the specular point approximation, it is important to add that the comparison must not be pushed too far in the case of a sea surface with multi sinusoid components. In the same way as for the monochromatic sea surface (see Figure 10), Figure 16 shows the TFR of the electromagnetic field computed using the specular point source model. Overall, this image has many features in common with Figure 14. However, significant differences can be pointed out between both images. This can be explained largely by the fact that multi sinusoid components involve local curvatures upon the sea surface. So, the electromagnetic scattering induces multi path reflection and more complex interactions that are not taken into account by the specular point approximation.

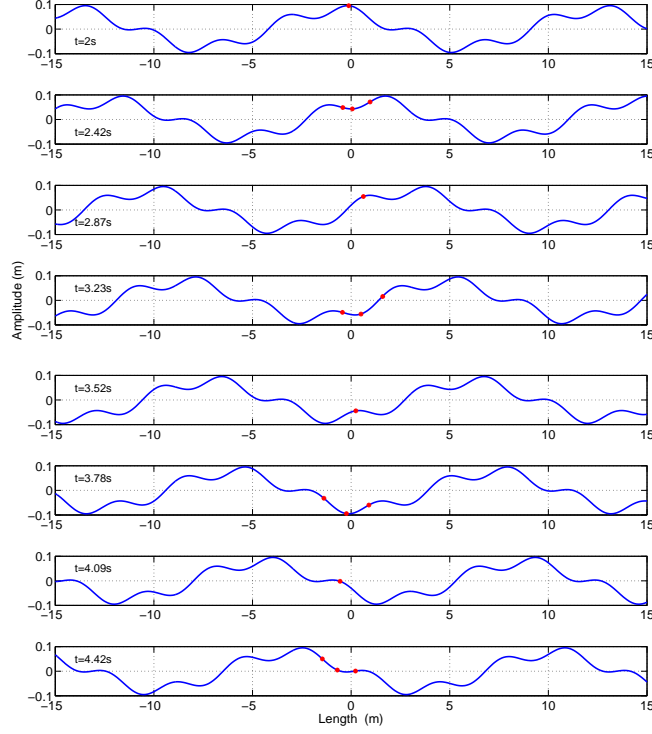


Figure 13: Sinusoidal surfaces and positions of the specular points at several times.

5.4 Surface made of three sinusoids

With a view to improving our sea surface model, the surface considered now consists of the sum of three sinusoids with different wavelengths and amplitudes and above all with different velocities. It is still considered a surface with parameters corresponding to Beaufort scale 3. The two added sinusoids are fixed so that the wavelength is respectively divided by 3 and 5, the amplitude is divided by 2 and 5 and the velocity is multiplied by 1.25 and 1.6.

In previous cases, the movement of the sea can be summarized into a global translation at a constant speed, see Figures 6 and 13. In reality, the sea surface has to be considered as a dispersive medium for the sea waves (speed depends upon the wavelength, see equation (7)). This dispersion induces deformations over time in addition to the translation. This last issue introduces new physical phenomena and modifies the TF features.

The TFR obtained for the three sinusoid models is presented in Figure 17. As in the case of two sinusoid models, the TFR allows us to view the micro-Doppler phenomena (oscillatory variations around the main trend). Nevertheless, the structure of these oscillations seems slightly more complex, in the present case.

Once again, to understand the TFR, we can make use of the specular point approximation. Figure 18 shows the TFR of the electromagnetic field approximated with the specular point source model. Despite significant differences, we do see that the global shape is very similar to Figure 17. Therefore the specular point approximation can, to large extent, provide a relevant description.

The TF representation for three sinusoid sea surfaces brings about quite complex phenomena that deserve more sustained analysis. Thus Figure 19 shows zooms of two areas of interest in Figure 17: from $t = 2\text{s}$ to $t = 3\text{s}$ and from $t = 6\text{s}$ to $t = 7.5\text{s}$. In addition, Figures 20 and 21 show the sea surface with the specular points at several successive times in these two periods.

Between $t = 2.13\text{s}$ and $t = 2.39\text{s}$ there is only one specular point inducing a Doppler curve that appears to be oscillating. In Figure 20, we can see that in a first step ($t = 2.13\text{s}/2.14\text{s}$) the specular point moves away from the receiver with a speed greater than the global sea movement. Then Doppler frequency is negative and lower than that obtained for a harmonic sea surface. In a second step ($t = 2.25\text{s}/2.26\text{s}$) the specular point locally tends to move closer to the receiver. The Doppler frequency increases and even reaches a positive

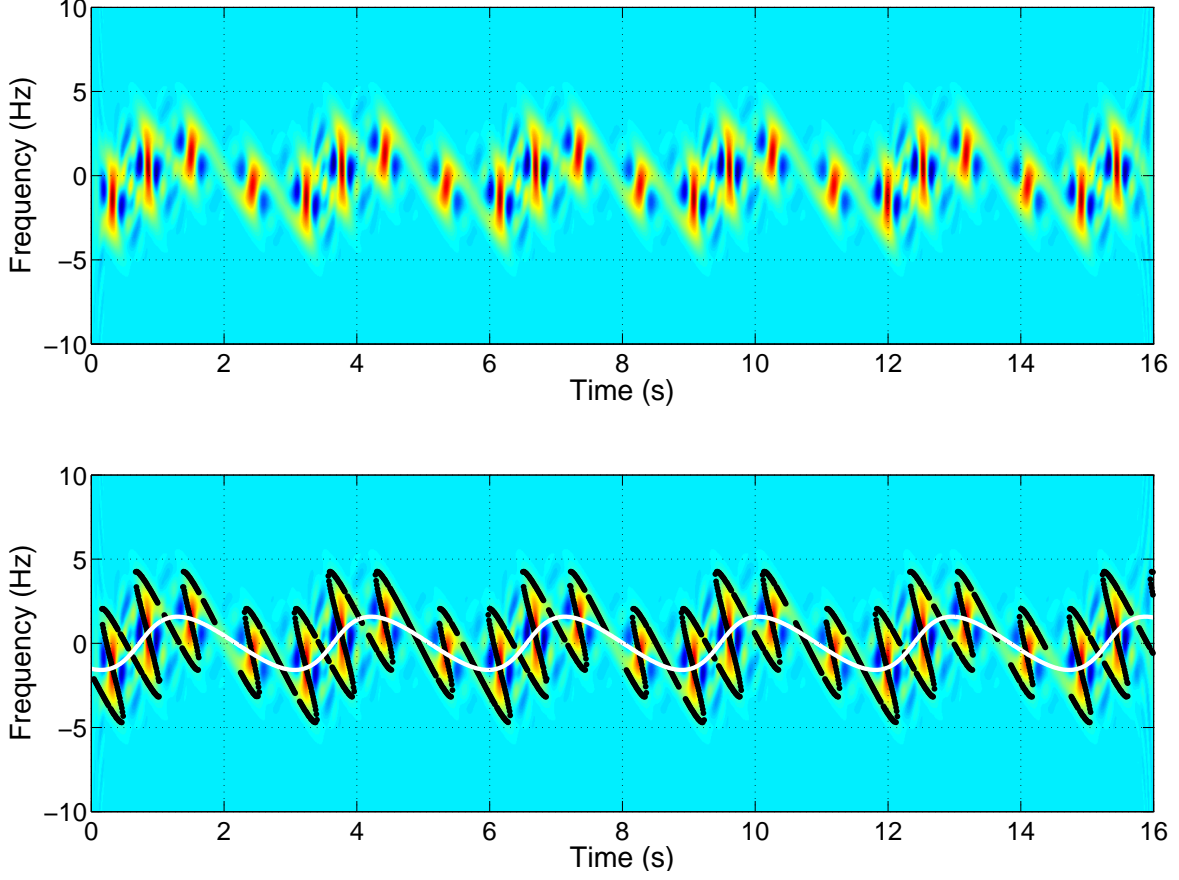


Figure 14: (top) TFR (with same color scale) of the signal reflected by the surface composed of two added sinusoids and (bottom) previous image including (black line) the Doppler of the specular points and (white line) the Doppler of the specular point of the corresponding simple sinusoidal surface (Figure 9).

maximum. In the last step ($t = 2.38\text{s}/2.39\text{s}$), the specular point speeds up the shift to the right, and Doppler frequency returns to negative domain. This oscillation cannot be explained by a global translation of the sea surface but must be seen as the consequence of the local sea surface deformations related to dispersion.

The deformations due to dispersion increase the complexity of the local curvature observed at the sea surface. Between $t = 6.21\text{s}$ and $t = 6.26\text{s}$, the number of specular points changes over time. Figure 21 shows that there is only one specular point from $t = 6.21\text{s}$ to $t = 6.22\text{s}$. Then, a new specular point appears at $t = 6.23\text{s}$. Finally this new point forks into two new specular points. Both specular points move closer to the observer but with different velocities. In the same way, we can see that dispersion and the local deformations of the sea surface periodically lead to the disappearance of one or more specular points. Somehow we must highlight the fact that the Doppler curves associated to each specular points still form a continuous Global Doppler curve.

6 Reflected signal in the TF domain - realistic sea surfaces

After considering the scattering by canonical surfaces, in this section, we investigate the TFR of the electromagnetic signal obtained for the scattering by realistic sea surfaces. Clearly, the surfaces generated using the theory presented in Section 3 are far more complex than those obtained using sinusoids or the sum of several sinusoidal functions. However, we are going to find most of the previous expounded phenomena that influence the time-frequency features.

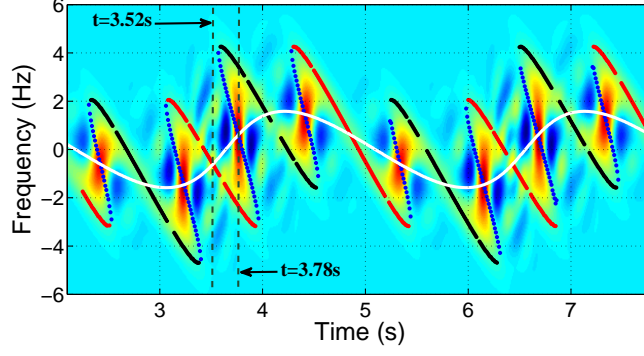


Figure 15: Zoom into Figure 14.b. Highlighted by the black, blue and red dots is the Doppler associated to each specular point and at each time.

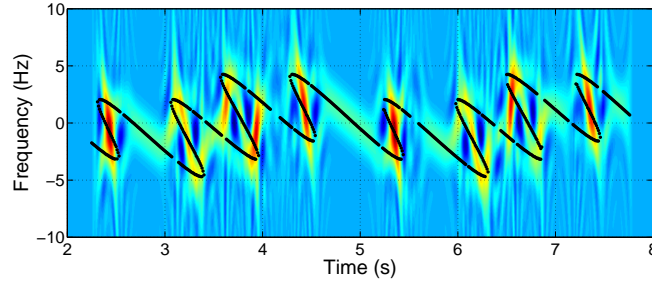


Figure 16: Zoom of the time-frequency representation of the received reflected signal by a surface made of the sum of two sinusoids using the point source model.

6.1 TFR of signals reflected by several sea surfaces

Figures 22 shows the TFR obtained from the signal reflected from sea surfaces with respectively Beaufort scale 2, 3 and 4. For the sea surface with Beaufort scale 2, from the receiver point of view, the surface is almost flat which is why the time frequency feature is mainly focused upon the zero-Doppler frequency line. The oscillations around this strip, which can be seen as micro-Doppler phenomena, are linked with the small oscillation of the surface. For the two other sea states, the surface can no longer be considered to be almost flat and then the TF feature appears as a far more structured geometry.

These TF representations suggest that there is great potential for feature extraction and specialized remote sensing applications. At first glance, we can see that the spreading of the Doppler frequency is in close conjunction with the sea state. This is illustrated in figure 23 which shows the (normalized) power distribution according to the Doppler frequency obtained from several sea states. It can also be notated that the micro-Doppler signature is directly related to the surface roughness and the fluid dynamics of the sea surface.

6.2 Analysis of the TFR for the sea surface at scale 3

Figure 24 shows the TFR and (stacked) the evolution (blue points) of the Doppler frequencies of the specular points. The Beaufort scale of the sea surface considered is 3.

It is clear that the understanding of this TFR image is much more complicated than canonical cases. Moreover, it is difficult to assert whether the Doppler curves related to each specular point form a continuous global curve in a present case. However, the cloud of points corresponding to each Doppler specular point bears similarities with the Doppler curve obtained in the two or three sinusoid surface cases.

In order to improve readability, Figure 25 focuses on a restricted time domain and Figure 26 represents the snapshots of the sea surface and the computed specular points (red stars) at specific times: $t = 6s$,

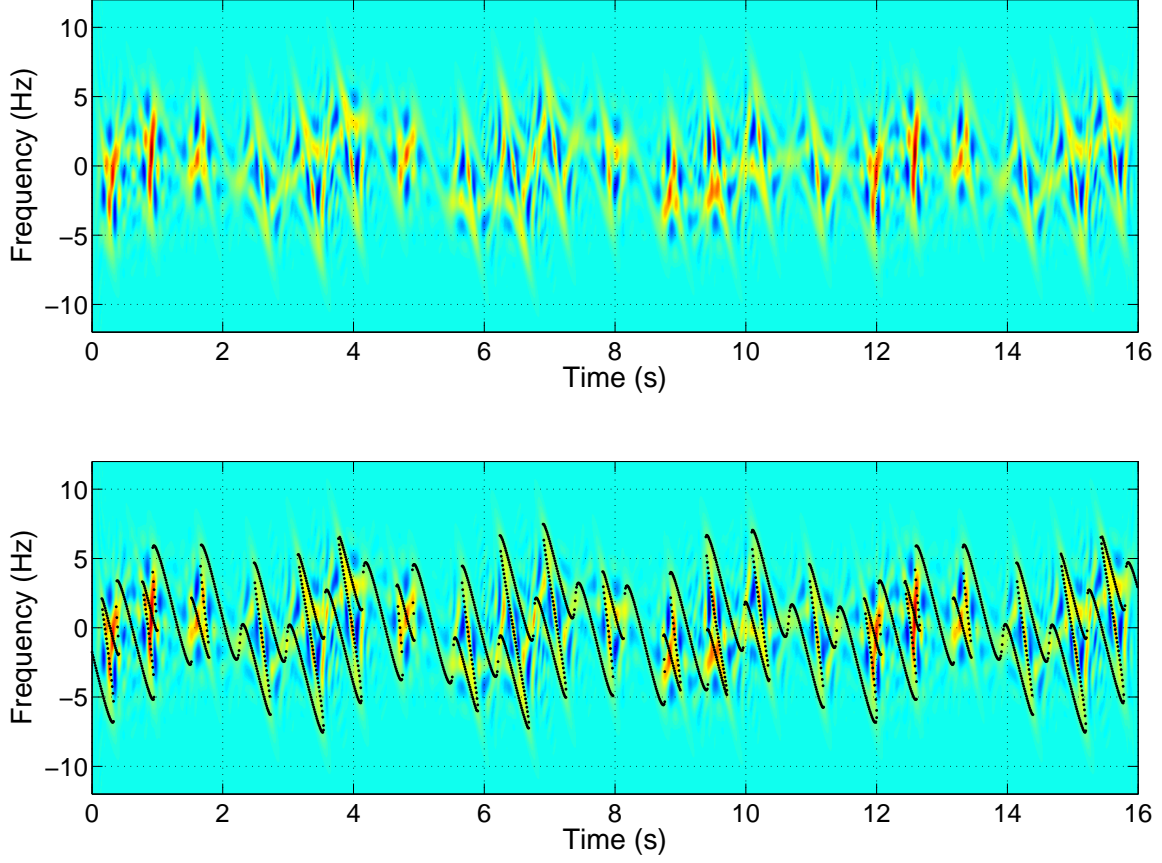


Figure 17: TF representation of the signal reflected from a surface made of the sum of three sinusoids with different velocities. In the bottom image the Doppler frequency due to the specular points is added (black dots).

$t = 6.48\text{s}$, $t = 7.48\text{s}$, $t = 8.64\text{s}$, $t = 10.46\text{s}$ and $t = 12.09\text{s}$.

First of all, it is noticeable that the TFR induced by a realistic sea surface looks like the Doppler curves observed in canonical cases at certain times ($t = 7.48\text{s}$ for instance). These situations most often occur when specular points are fewer and form a gathering of points as in Figure 26. In these situations, it becomes easy to make comparisons with the canonical cases previously studied and it may give rise to the very simple physical interpretations given in Section 5.

Conversely, when the distribution of the specular points spreads over a larger region (between $t = 6\text{s}$ and $t = 6.48\text{s}$), the time frequency signature becomes more complex and is probably the consequence of multi-scale phenomena. Furthermore, Figure 26 shows that realistic sea surfaces often cause non uniform specular point distributions. In certain cases, the distribution of specular points is structured as different clusters. In the latter case, the TFR is characterized by multi component electromagnetic interactions.

In any case, it is reasonable to assume that deterministic or statistical analysis of the TFR related to a given sea surface could provide significant information about the fluid dynamics of the sea. In a first instance, the analysis could consist in an extraction of the global TFR structure (pseudo periodic structure). In a second phase, the analysis could focus upon the specific TFR structures related to the multi-scale phenomena. Progress will be made in future works on this matter.

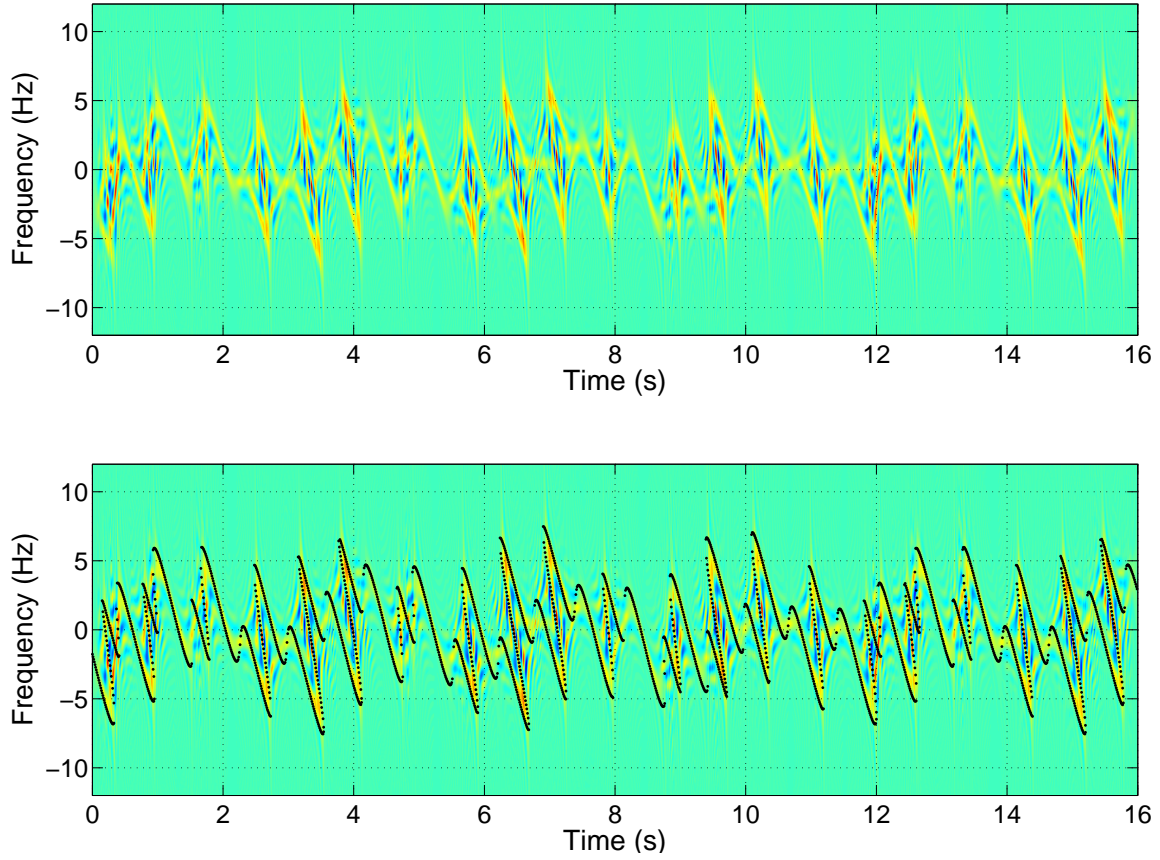


Figure 18: TF representation of the signal (point source approach) reflected from a surface made of the sum of three sinusoid with different velocities. In the bottom image the Doppler frequency due to the specular points added using black dots.

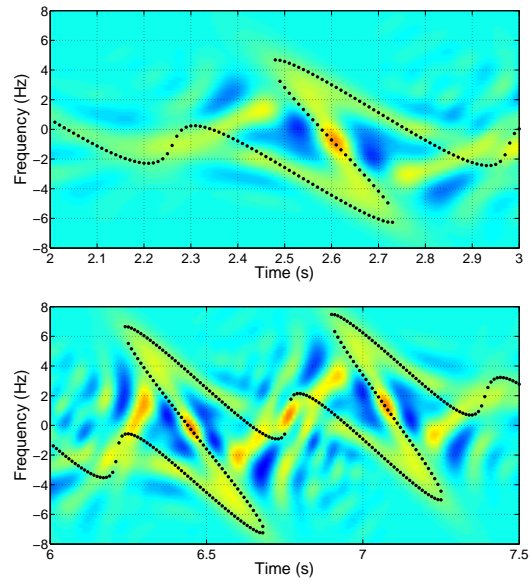


Figure 19: Zoom on an area of interest in Figure 17.

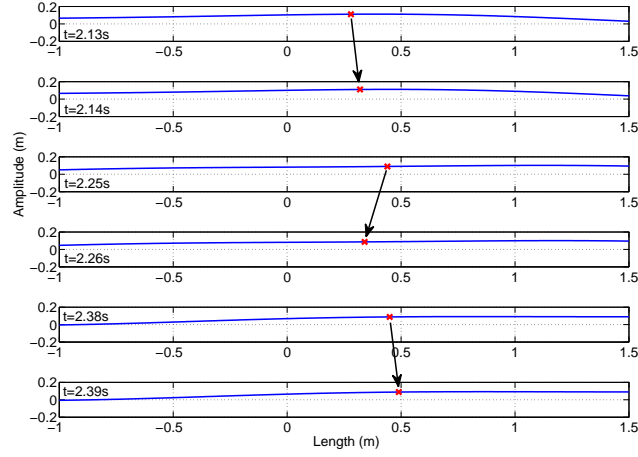


Figure 20: Three sets of two (zoom) successive surfaces (blue line) and the evolving positions (shown by the black arrows) of the specular point (red star).

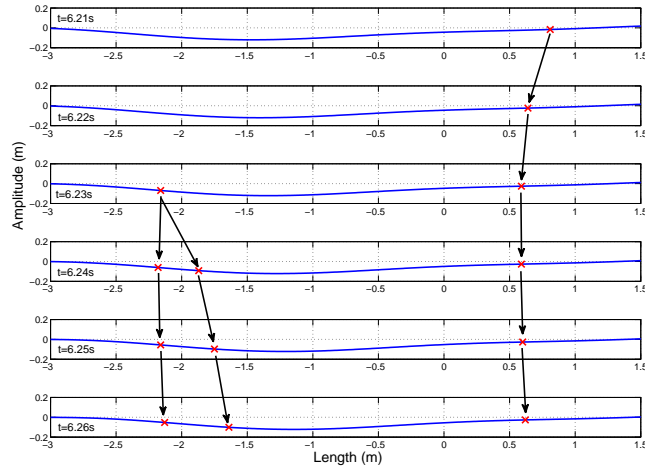


Figure 21: Example showing (zoom) six successive surface shapes (blue line) and the evolving positions (shown by the black arrow) of the specular points (red star).

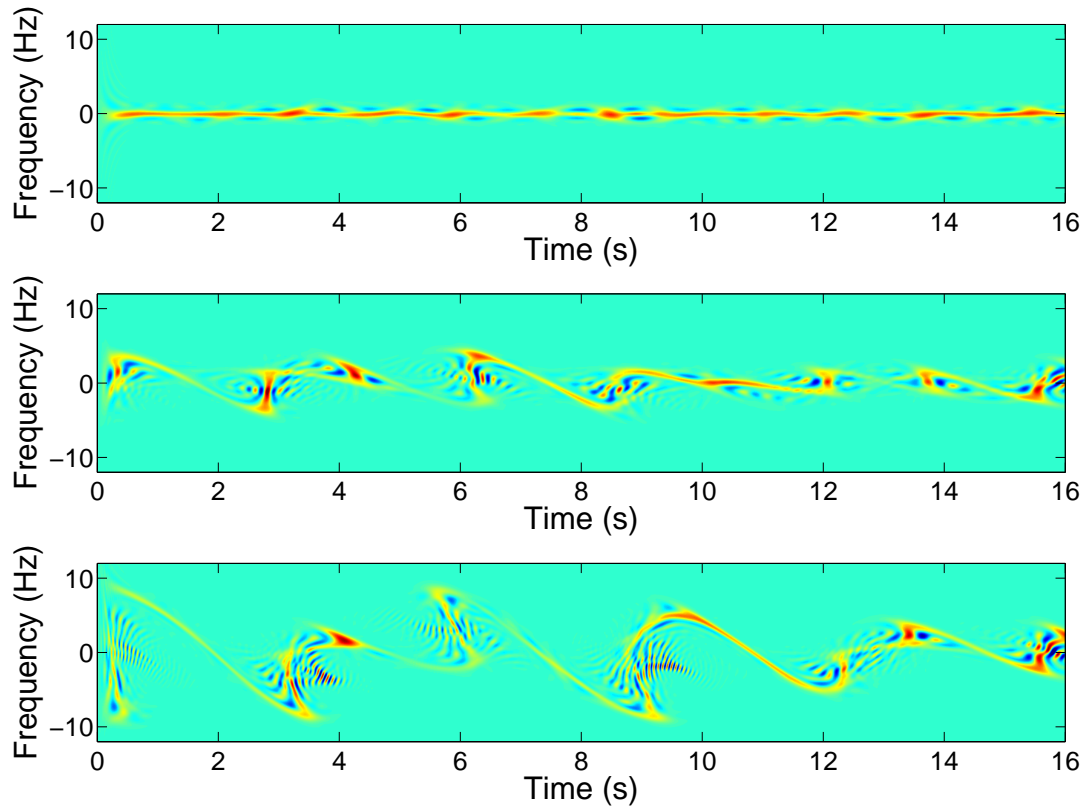


Figure 22: TF representation of the signal reflected from a sea state with scale (top to bottom) 2, 3 and 4.

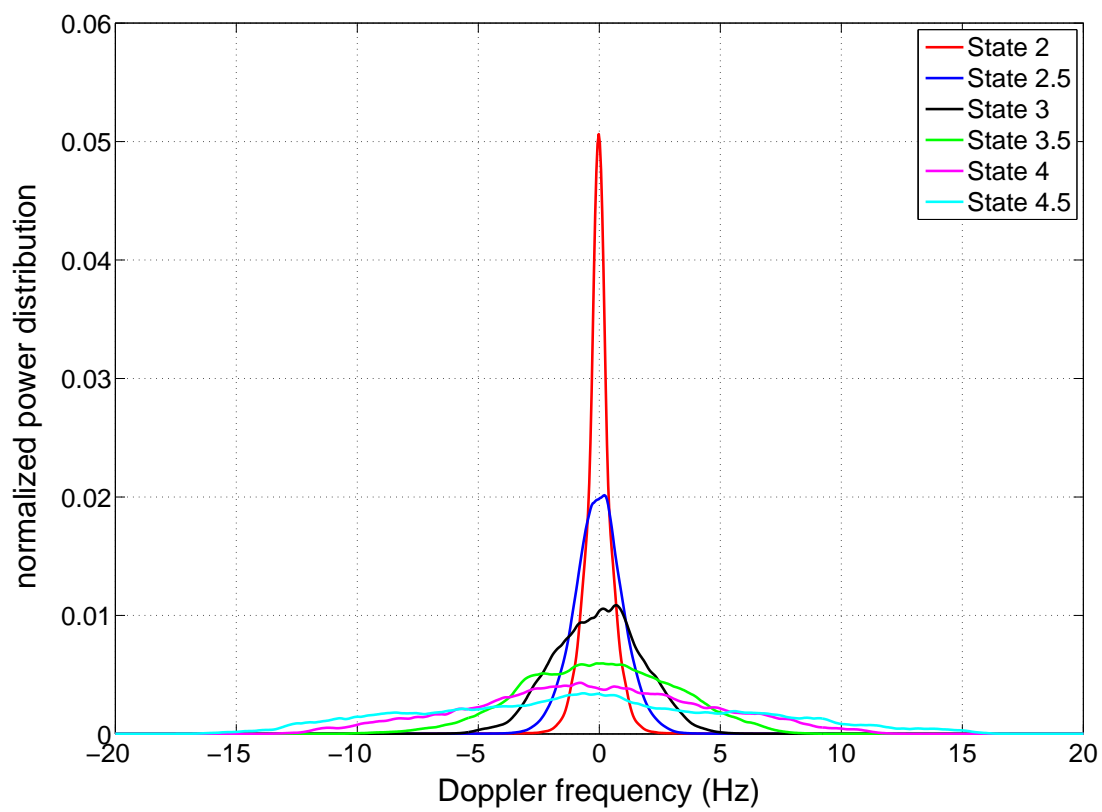


Figure 23: Normalized power distribution for several sea states.

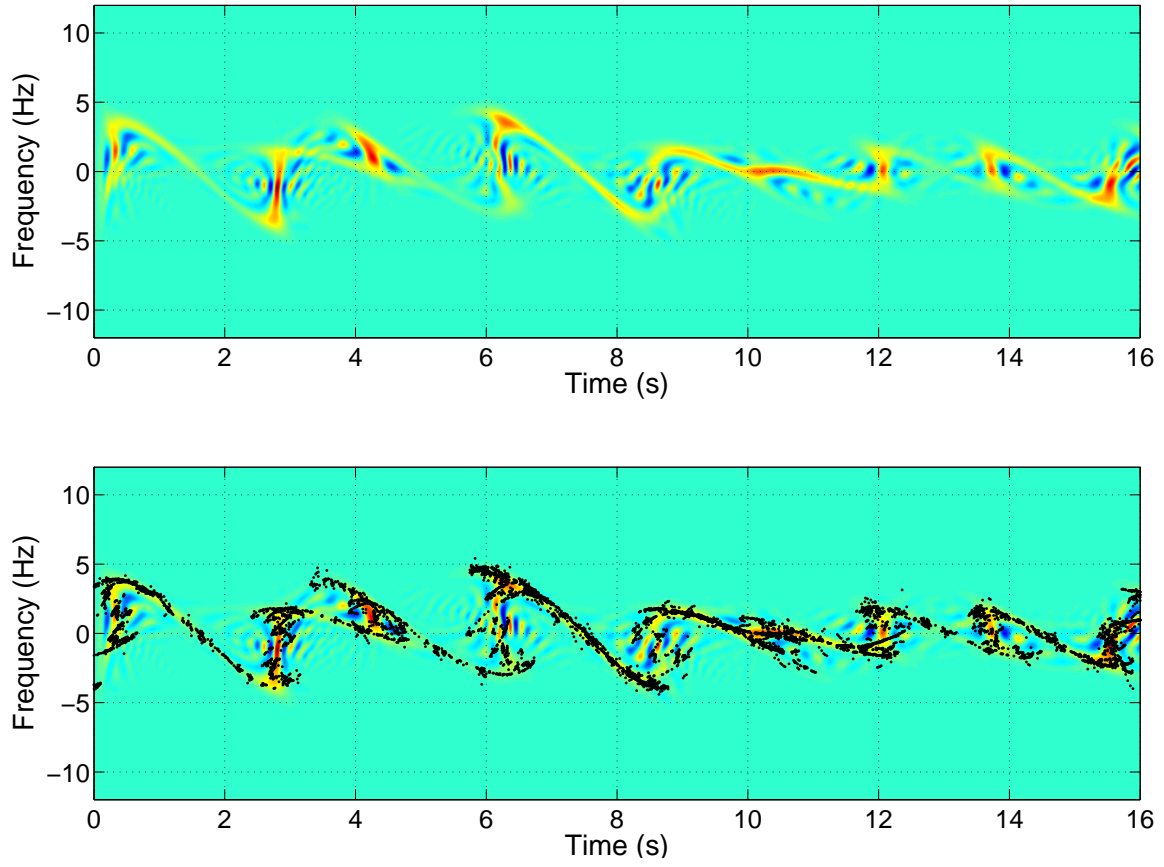


Figure 24: TF representation of the signal reflected from a sea surface with state scale 3 and the frequency Doppler of the specular points (black dots).

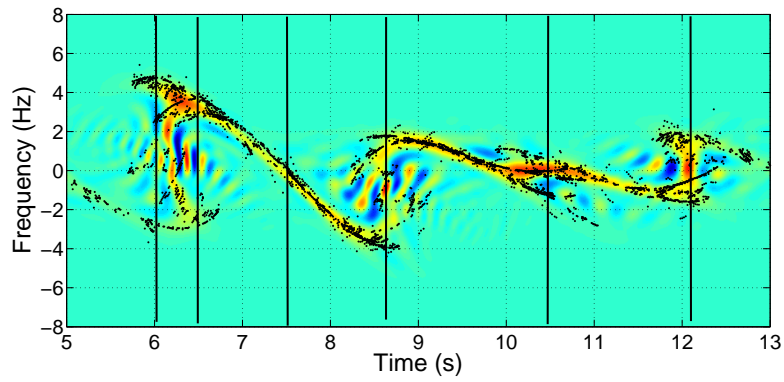


Figure 25: Zoom of Figure 24. Black lines show the times corresponding to the sea surface drawn in Figure 26.

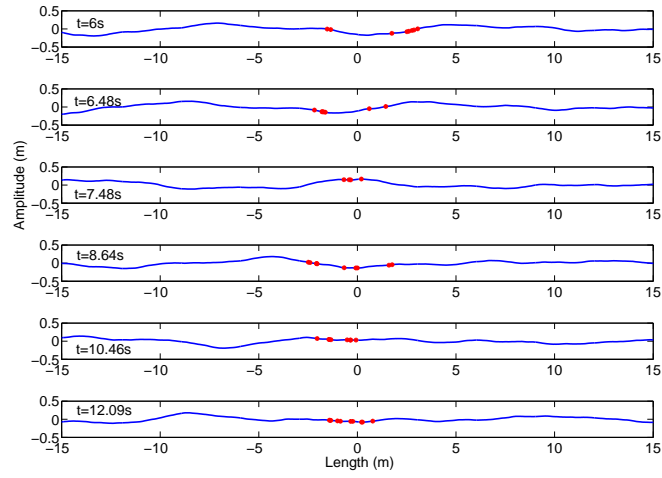


Figure 26: Sea surface at several times and in red the positions of the specular points.

7 Conclusion

This paper investigates the feature in the time-frequency domain of L-band signals reflected from sea surfaces. The data used have been generated using a MoM method and the TFR have been obtained from the TFTB toolbox. It has been shown that the signatures of the reflected signals in the TF domain are linked with the physics of the fluid dynamics. These proposed results provide the basis for interpreting the scattering of L-band waves by time varying sea surfaces. More precisely, it has been shown that the specific patterns (looking like sigmoid functions) can be linked to the specular reflections of the incident wave on the sea surface. In addition, we have seen that local oscillations of the time frequency curve could be related to dispersion phenomena of the fluid surface. This preliminary study opens up new opportunities for GNSS signals (L-band signals) as remote sensing systems for dynamic sea surfaces.

Future works will focus on the estimation of oceanographic parameters from these time-frequency analyses of reflected signals. Eventually, this study will later be extended to the analysis of non-linear sea or breaking waves [19].

Acknowledgment

This work was supported by ‘GIS Europôle Mer’ and ENSTA Bretagne.

References

- [1] M. Belmonte Rivas and M. Martin-Neira. Coherent GPS reflections from the sea surface. *IEEE Geoscience and Remote Sensing Letters*, 3(1):28–31, 2006.
- [2] J. F. Marchan-Hernandez, M. Vall-llossera, A. Camps, N. Rodriguez-Alvarez, I. Ramos-Perez, E. Valencia, X. Bosch-Lluis, M. Talone, J. M. Tarongi, and M. Piles. Ground-based GNSS-R measurements with the PAU instrument and their application to the sea surface salinity retrieval: First results. In *IEEE International Geoscience and Remote Sensing Symposium (IGARSS)*, volume 4, pages 530–533, 2008.
- [3] J. L. Garrison, J. K. Voo, S. H. Yueh, M. S. Grant, A. G. Fore, and J. S. Haase. Estimation of sea surface roughness effects in microwave radiometric measurements of salinity using reflected global navigation satellite system signals. *IEEE Geoscience and Remote Sensing Letters*, 8(6):1170–1174, 2011.
- [4] D. K. Yang, Y. Q. Zhang, Y. Lu, and Q. S. Zhang. GPS reflections for sea surface wind speed measurement. *IEEE Geoscience and Remote Sensing Letters*, 5(4):569–572, 2008.
- [5] J. K. Voo, J. L. Garrison, S. H. Yueh, M. S. Grant, A. G. Fore, J. S. Haase, and B. Clauss. Application of reflected global navigation satellite system (GNSS-R) signals in the estimation of sea roughness effects in microwave radiometry. In *11th Specialist Meeting on Microwave Radiometry and Remote Sensing of the Environment (MicroRad)*, pages 140–145, 2010.
- [6] V.U. Zavorotny, A.G. Voronovich, S.J. Katzberg, J.L. Garrison, and A. Komjathy. Extraction of sea state and wind speed from reflected GPS signals: Modeling and aircraft measurements. In *IEEE International Geoscience and Remote Sensing Symposium (IGARSS)*, volume 4, pages 1507–1509, 2000.
- [7] J. L. Garrison, A. Komjathy, V. U. Zavorotny, and S. J. Katzberg. Wind speed measurement using forward scattered GPS signals. *IEEE Trans. Geoscience and Remote Sensing*, 40(1):50–65, 2002.
- [8] V. U. Komjathy, A. and Zavorotny, P. Axelrad, G. H. Born, and J. L. Garrison. GPS signal scattering from sea surface: Wind speed retrieval using experimental data and theoretical model. *Remote Sensing of Environment*, 73(2):162–174, 2000.
- [9] V. U. Zavorotny and A. G. Voronovich. Scattering of GPS signals from the ocean with wind remote sensing application. *IEEE Trans. Geoscience and Remote Sensing*, 38(2):951–964, 2000.

- [10] D. R. Thompson, L. A. Linstrom, R. F. Gasparovic, and T. M. Elfouhaily. Surface roughness estimation from GPS sea reflections. In *IEEE International Geoscience and Remote Sensing Symposium (IGARSS)*, volume 2, pages 1278–1280, 2002.
- [11] A. Coatanhay, R. Garelo, B. Chapron, and F. Ardhuin. Project MOPS - Marine Opportunity Passive Systems. In *Passive'08*, Hyères, 2008.
- [12] W. Gibson. *The Method of Moments in Electromagnetics*. Chapman & Hall/CRC, 2008.
- [13] E. I. Thorsos. The validity of the kirchhoff approximation for rough surface scattering using a gaussian roughness spectrum. *Journal of the Acoustical Society of America*, 83(1):78–92, 1988.
- [14] L. Tsang, J. A. Kong, K.-H. Ding, and C. O. Ao. *Scattering of electromagnetic waves. Numerical simulations*. John Wiley & Sons, 2001.
- [15] T. Elfouhaily, B. Chapron, K. Katsaros, and D. Vandemark. A unified directional spectrum for long and short wind-driven waves. *J. of Geophysical Research*, 102(C7):15781–15796, 1997.
- [16] B. Boashash. *Time-Frequency Signal Analysis and Processing. A Comprehensive Review*. Elsevier, 2003.
- [17] V. C. Chen, F. Li, S-S. Ho, and H. Wechsler. Micro-Doppler effect in radar: Phenomenon, model, and simulation study. *IEEE trans. Aerospace and Electronic Systems*, 42(1):2–21, 2006.
- [18] T. Thayaparan, S. Abrol, and E. Riseborough. Micro-Doppler radar signatures for intelligent target recognition. Technical Report TM 2004-170, Defence R&D Canada - Ottawa, 2004.
- [19] R. Khairi, A. Coatanhay, A. Khenchaf, and Y.-M. Scolan. Numerical modeling of electromagnetic waves scattering from 2d coastal breaking sea waves. *The European Physical Journal Applied Physics*, eFirst, 2013.